CHEMISTRY OF MATERIALS

Open Access

pubs.acs.org/cm

Article

High-Throughput Screening of All-*d*-Metal Heusler Alloys for Magnetocaloric Applications

Nuno M. Fortunato,* Xiaoqing Li, Stephan Schönecker, Ruiwen Xie, Andreas Taubel, Franziska Scheibel, Ingo Opahle, Oliver Gutfleisch, and Hongbin Zhang*

Cite This: *Chem. Mater.* 2024, 36, 6765−6776

Read Online

ACCESS | Metrics & More | Article Recommendations | Supporting Information

ABSTRACT: Due to their versatile composition and customizable properties, A_2BC Heusler alloys have found applications in magnetic refrigeration, magnetic shape memory effects, permanent magnets, and spintronic devices. The discovery of all-*d*-metal Heusler alloys with improved mechanical properties compared to those containing main group elements presents an opportunity to engineer Heusler alloys for energy-related applications. Using high-throughput density-functional theory calculations, we screened magnetic all-*d*-metal Heusler compounds and identified 686 (meta)stable compounds. Our detailed analysis revealed that the inverse Heusler structure is preferred when the electronegativity difference between the A and B/C atoms is small, contrary to conventional Heusler alloys. Additionally, our calculations of Pugh ratios and Cauchy pressures demonstrated that ductile and metallic bonding are widespread in all-*d*-metal Heuslers, supporting their enhanced mechanical behavior. We identified 49 compounds with a double-well energy surface based on Bain path calculations and magnetic ground states, indicating their potential as candidates for magnetocaloric and shape memory applications. Furthermore, by calculating the free energies, we propose that 11 compounds exhibit structural phase transitions and suggest isostructural substitutions to enhance the magnetocaloric effect.

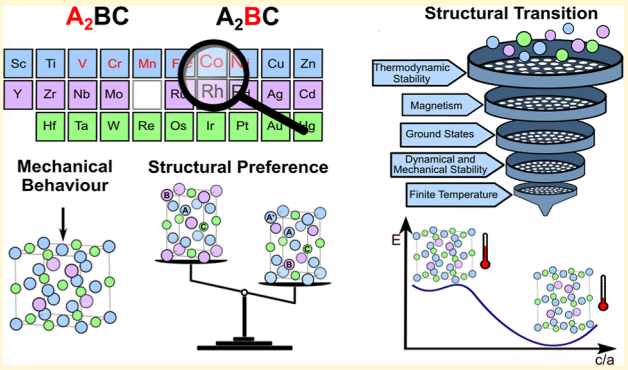

INTRODUCTION

Heusler alloys exhibit a wide range of stable compounds with an A_2BC stoichiometry, forming a crystal structure comprising rock salt (AB and AC) and cubic (AA' and BC) sublattices.[1] This leads to a wide spectrum of physical properties and promising applications, e.g., magnetic refrigeration,[2,3] permanent magnets,[4] magnetic shape memory (MSM) effect,[5] and spintronic devices.[6] Conventionally, A and B are metallic elements and C is a main group element, resulting in the coexistence of covalent, ionic, and metallic bonds.[1,7] From the structural point of view, in addition to the regular Heusler structure with $L2_1$-type ($Fm\bar{3}m$, spg. n° 225), Heusler alloys also occur in the XA-type ($F\bar{4}3m$, spg. n° 216), dubbed as inverse Heuslers, along with the tetragonal variants of both structures, i.e., in the *I*4/*mmm* (spg n° 139) and $I\bar{4}m2$ (spg n° 119) space groups, respectively. The inverse Heusler type can be obtained by exchanging the occupation of one of the A sites with the B-site element, resulting in two inequivalent A sites, as exemplified in Figure 1 (a). Burch et al. observed that in $Fe_{3-x}TM_xSi$ (TM = transition metal) the TM dopant adopts the A Fe-sites if it belongs to the same or later periodic group than Fe (similar occupation to inverse Heusler), while earlier elements prefer the B Fe-sites (as in regular Heuslers alloys), this is known as Burch's rule.[8]

Furthermore, the relative stability between tetragonal and cubic structures in Heusler alloys, as described by the Bain path,[9] can lead to a martensitic phase transition,[10] as sketched in Figure 1(b). For instance, Ni−Mn-X (X = Al, Ga, In, and Sn) Heusler alloys host a first-order structural transition where the metastable cubic $Fm\bar{3}m$ structure acts as a high-temperature (austenite) phase that on cooling transforms to the ground state *I*4/*mmm* martensite phase and also lower symmetry modulated martensite phase can occur dependent on the chemical composition.[11] A magnetostructural transformation involves both a structural change between the martensite and austenite phases, and a change in magnetic state, for instance, the transition from paramagnetic to ferromagnetic (FM) in Co−Ni−Mn−In.[12] A magnetostructural transformation can be induced by an externally applied magnetic field owing to the stabilization of the FM phase,

Received: February 6, 2024
Revised: April 18, 2024
Accepted: April 19, 2024
Published: July 1, 2024

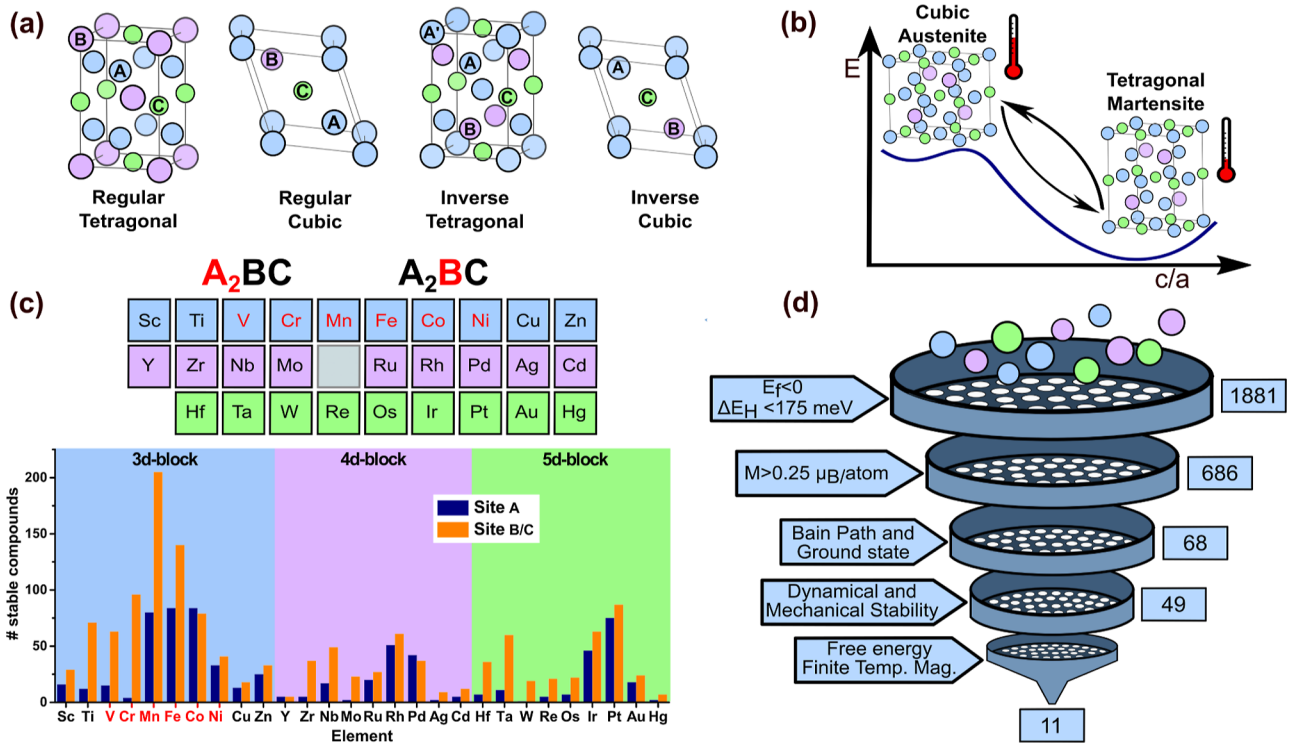

Figure 1. Crystal structures in our HTP search, the inverse/regular cubic Heuslers in their primitive setting, and the inverse/regular in their tetragonal setting. (b) A schematic of how the Bain path relates to the structural transition of low temperature tetragonal (ground state) martensite to the high-temperature cubic austenite. (c) The compositional phase space of our HTP, the graph below shows the frequency of elements in our stable magnetic compounds in the resulting screening. (d) The summary of our HTP results showing each step of the screening procedure and the respective number of compounds remaining.

which can be used for magnetocaloric cooling. A further interesting application is MSM alloys.

More recently, Wei et al.[13] synthesized $Ni_2Mn_xTi_{1-x}$ Heusler alloys, which are notably composed only of *d*-metals, omitting the main group elements on the C site. As in Ni−Mn-X alloys, the magnetostructural transition in $Ni_2Mn_xTi_{1-x}$ can be tailored by the Mn content, which also changes the valence electron per atom ratio (e/a). In addition Co-doping can be used to stabilize the FM state and increase the magnetization.[13,14] Of note, the all-*d*-metal Co−Ni−Mn−Ti alloy exhibits better mechanical stability during repeated structural transitions, in comparison to the more brittle conventional Ni−Mn-X Heuslers, which has been attributed to the *d*−*d* hybridization.[15−18] This makes all-*d*-metal alloys promising for MSMs, magnetocaloric, barocaloric, and elastocaloric applications.

Thus, all-*d*-metal Heuslers standout as a promising candidate system for cooling cycles based on the magnetocaloric effect (MCE), for example, by exploiting hysteresis using a simultaneous application of stress and field.[19] In addition, the tunability of the electronic structure of all-*d*-metal Heuslers also open up new functionalities and applications. For instance, large magnetoresistance values were found in Co−Ni−Mn−Ti and Ni−Co−Mn(Cu)−Ti,[20,21] due to the resistance doping significantly upon transition to the austenite phase, at the same time Ni-(FeCo)−Mn−Ti shows giant exchange bias[22] due to the coexistence of antiferromagnetic (AFM) and FM exchange interactions. Whereas, Co_2VMn exhibits a tunable eg orbital occupancy, which makes them interesting as electrocatalysts for oxygen evolution reactions.[23] Thus, the all-*d*-metal Heuslers are a new twist in the Heusler family and have brought fresh attention to this material class, as potential novel materials and their technological applications.[24]

Density functional theory (DFT) calculations have been used to shed light on the structural, mechanical, and electronic behavior of all-*d*-metal Heuslers. Such as the magneto-structural transition and mechanical properties of Co−Ni−Mn−Ti, including under different doping elements such as Fe, Cu, and interstitial boron.[25−30] The possibility of martensitic transitions were discussed for several families of compounds including TM_2MnTi (TM = Pd, Pt, Ag, Au, Cu, and Ni),[31] $TM_{2-x}Mn_{1+x}V$ (TM = Pd, Ni, Pt, Ag, Au, Ir, and Co; x = 1,0),[32] and Zn_2MnTM (TM = Ru, Rh, Pd, Os, and Ir);[33] however, thermodynamic stability was not provided. Notably, Li et al. discussed the mechanical and electronic properties of the Ni_2MnTM (TM = Sc, Ti, V, Cr, Y, Zr, Nb, Mo, Hf, Ta, and W) family, remarking that early elements favor the conventional Heusler structure.[34] Since formation energies and distance to the convex Hull are absent in studies of all-*d*-metal Heuslers, there is a need for a thermodynamic screening over the whole compositional space that systematic accounts for different magnetic ground structures and structures. Furthermore, while there is an emphasis on discussing the possibility of a transition, a discussion of finite-temperature properties is lacking.

High-throughput (HTP) screening based on DFT has been widely used to design Heusler alloys by exploring their versatile chemical space.[35,36] For instance, Sanvito et al.[37] performed a screening of compositions with *d*-block and main group elements, finding 248 compounds that were labeled as thermodynamically stable. From these, several candidates were synthesized as a trial: Co_2MnTi, Mn_2PtPd, Mn_2PtCo,

https://doi.org/10.1021/acs.chemmater.4c00345
Chem. Mater. 2024, 36, 6765−6776

and Mn_2PtV. Of note, the tetragonally distorted structures were only considered in the 248 compounds that were stable in the cubic phase. Moreover, Balluff and colleagues[38] carried out screening of the AFM ground states of Heusler compounds for spintronic applications, and predicted 21 compounds with Néel temperatures (T_N) above room temperature.

Additionally, there have been extensive HTP screenings focusing on the nonmagnetic Heusler alloys and their possible applications, such as Heuslers as precipitates/alloy systems to improve the mechanical behavior[39] and energy generation using the thermoelectric effect.[40] While Faleev and colleagues[41] used HTP calculations to argue that tetragonality correlates with features in the electronic structure of the corresponding cubic structures.

A different approach was made by Oliynyk et al.[42] that constructed a machine-learning model trained on crystallographic databases to predict the synthesizability of regular and inverse Heusler alloys, where new Ru−Ga-X (X = Ti−Co) Heusler alloys were successfully synthesized based on their models.

We have recently published the anomalous Hall and Nernst conductivity of FM all-*d*-metal regular Heusler compounds,[43] and in this work, we detail the HTP screening of magnetic all-*d*-metal Heuslers. We shed light on the compositional range, ground state structures, and in particular, the mechanical and thermodynamic behavior of all-*d*-metal Heuslers, based on a workflow for the discovery of materials for energy applications, namely, MCE and MSM alloys.[44] From the thermodynamic stability, we predict 686 (meta-)stable compounds and identify their magnetic/structural ground states. Using such an extensive data set, we rationalize how intermetallic bonding affects the structural preference between regular and inverse Heusler structures as dictated by Burch's rule and correlate the bonding behavior with the mechanical behavior. Furthermore, following the concept of the Bain path and the relative stability of the tetragonal and cubic phases, we screen such compounds for possible magneto-structural transitions by evaluating their finite temperature magnetic and structural behavior. Finally, we provide a path for the tuning of phase transition behavior necessary for optimal MCE applications. This paves the way to design and optimize novel functional materials for (magnetic) shape memory and (magneto-)caloric applications.

METHODS

The HTP relaxation and total energy DFT calculations were performed using the Vienna ab initio code (VASP)[45,46] within an in-house HTP code,[47] the exchange correlation was treated using the PBE functional.[48] For the HTP screening, the four-atom primitive cell for the $L2_1$ and XA structures were used, along with the conventional unit cell of the *I*4/*mmm* and I $\bar{4}$ m2 structures initialized at c/a = 1.35 and then relaxed. The cutoff energy of the plane waves was set to 550 eV and for the *k*-mesh VASP's automatic scheme was used, which generates a Gamma-centered Monkhorst−Pack grid with the k-mesh density set to 35, i.e., the number of *k*-points in each direction is approximately 35 multiplied by the reciprocal lattice vector. The HTP AFM screening procedure was performed by considering different AFM configurations within an eight-atom cell for both cubic and tetragonal systems, which were relaxed in the AFM state. For systems with $E_{AFM} < E_{FM}$, we systematically perform the AFM Bain path. The FM and AFM Bain paths were calculated using energy values from a Birch−Murnaghan fit of the energy−volume curve at a constant c/a ratio.

The phonon stability and QHA vibrational free energies were obtained using the frozen phonon approach in phonopy[49] in 64 atom supercells, with the electronic contribution included using the fixed Density of States method, the volumes were calculated in 1.5% steps. Forces were calculated using VASP, with a k-mesh density of 50 and an energy cutoff of 540 eV. The single crystal elastic constants were calculated with a plane-wave cutoff of 700 eV, using VASP's built-in stress−strain method. Both calculations were carried out in the respective magnetic ground state of the structure, with a convergence criterion of 10^{-7} eV. With the same settings the LOBSTER code[50−52] was used to calculate the COHP for selected compounds.

Magnetic exchange interactions[53] were calculated within a radius of 4 lattice parameters using the SPR-KKR code[54,55] by applying the magnetic force theorem to the converged electronic structure of the magnetic ground state found earlier on. The angular moment cutoff of the spherical harmonics was set to $l = 3$ and a *k*-mesh density was approximately 2000 points per irreducible Brillouin zone wedge. When electronic convergence was not achieved in SPRKKR, it was replaced by the JuelichKKR code at comparable settings.[56] The Currie temperature calculation by Monte Carlo Metropolis sampling, within a 10 × 10 × 10 supercell and the Curie temperature was determined by using the Binder cumulant in FM systems and heat capacity peak for AFM cases. The Bain paths of selected disordered systems were calculated using the Coherent Potential Approximation (CPA) as implemented in the EMTO−CPA code, which based on an all-electron Exact Muffin-Tin Orbitals formalism.[57−63] The PBE functional was used along with soft-core approximation and 13 × 13 × 13 *k*-mesh. For the A-site, the ASA atomic sphere size was 1.08 that of the Wigner-Seitz spheres and the scale of potential spheres was chosen to be 0.95, while for other sites, both values were set to 1.00.

RESULTS

Thermodynamic Stabilities. The compositional range of our HTP screening covers the whole *d*-element block (excepting Tc) with at least one magnetic 3*d* atom (V, Cr, Mn, Fe, Co, and Ni) on either the A or B/C sites (see Figure 1c), resulting in a total of 5802 unique compositions. For each composition, we consider four different structures: the primitive four-atom regular and inverse Heusler cells, (i.e., $L2_1$ and XA types) and the two respective eight-atom tetragonally distorted structures (i.e., with space groups of *I*4/*mmm* and I $\bar{4}$ m2), in both the FM and nonmagnetic settings. In total, we find 2482 ternary compositions with a negative formation energy (E_f) and 1881 with a distance to the convex Hull (ΔE_H) lower than 175 meV/atom. The frequency of occurrence for each element in those 1881 compounds is shown in Figure 1c. Obviously, among the 3*d* magnetic elements, Fe, Co, and Mn are the most common elements due to the constraint of the compositional space. Whereas among the 4*d* and 5*d* blocks, there are two maxima that occur at groups 5 (Nb,Ta) and 9−10 (Rh, Ir, Pd, and Pt) tapering off at the late, early, and in-between elements.

Strictly speaking, a system is expected to be stable if it is on the convex Hull ($\Delta E_H = 0$); however, in practice, a cutoff is usually allowed, so that the metastable phases are also considered.[35] To ensure interesting magnetic properties, we focus only on compounds, where either the cubic or tetragonal settings are magnetic, chosen as a magnetic moment larger than 0.25 μ_B.atom^{-1}, further reducing to 686 stable ternary all-*d*-metal Heusler compounds. With more than half below a 75 meV/atom distance to convex Hull (cf., Table S.1).

Our results can be well validated with the experimentally available cases (see Table S.2 for a comparison). For instance, the $L2_1$ structure of Ni_2MnTi has a large ΔE_H of 117 meV/atom, which can be attributed to the fact that the experimental phase is a B_2-disordered phase[14,64] and finite temperature effects. Likewise, Co_2VMn reported by Yu et al.[23] is 67 meV/atom above the convex hull, again indicating that the all-*d*-

https://doi.org/10.1021/acs.chemmater.4c00345
Chem. Mater. 2024, 36, 6765−6776

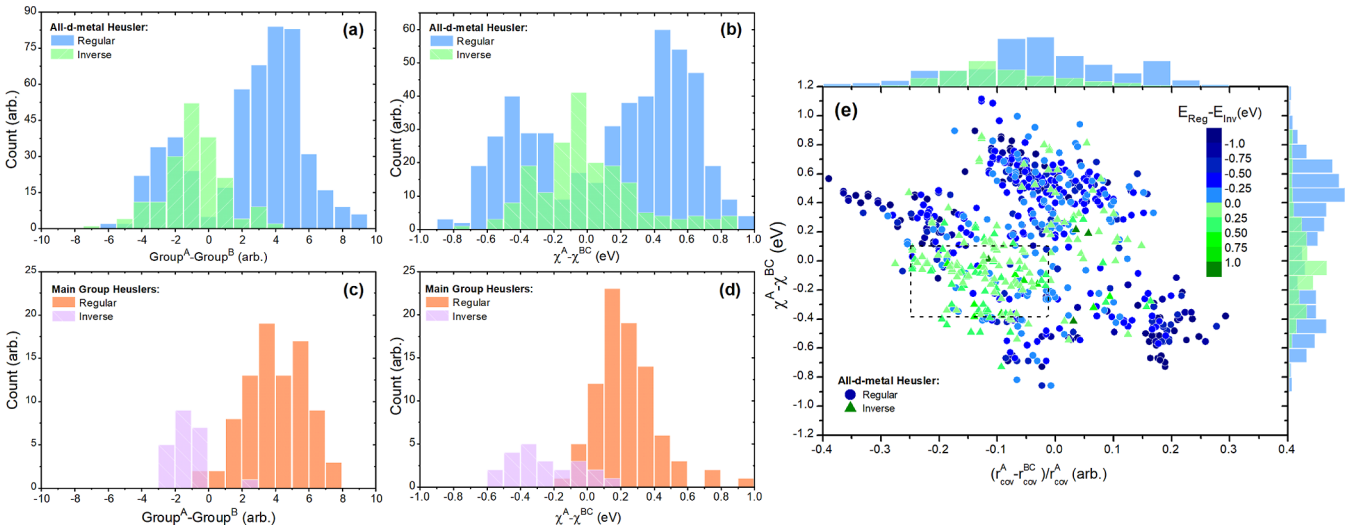

Figure 2. (a) Histogram showing the frequency of occurrence of regular (in blue) and inverse (green with stripes) all-*d*-metal Heusler structures as a function of the difference in group number of A and B elements. (b) The difference between the electronegativity of the A element and the average of B and C elements as a histogram. (c) The difference in group number of A and B elements applied to Heuslers with main group elements in literature. (d) The electronegativity difference histogram for Heusler with main group elements. (e) Map of the regular (circle) and inverse (triangle) structures as a function of electronegativity and radius of A elements and the average of the B and C atoms. Color indicates the energy difference between both structures, and dashed lines delineate the region where the inverse Heusler structure is most prevalent. On top of each axis we plot the respective histogram for the radius and electronegativity differences.

metal Heuslers can still be synthesized even if they have a relatively large ΔE_H. At the same time, both Mn_2PdPt and Co_2MnTi are on the convex hull, and we find good agreement with the available experimental lattice parameters (see Table S.2).[37] While Mn_2PdPt exhibits an AFM ordering[37] leading to a small deviation in the lattice parameter, which is improved by considering FM states, as done below. Of note, Mn_2PtCo and Mn_2PtV were found to decompose to binaries by Sanvito et al.,[37] with the former being 10 meV/atom and the latter 28 meV/atom above the convex hull. Based on these cases and given the possibility of AFM ordering (discussed below) that could lower the total energies, or disorder that adds a configurational entropy term,[65] we consider that the 175 meV/atom tolerance of distance to the convex hull as a necessity to allow the inclusion of metastable compounds of interest. In particular, the small differences between electronegativities and ionic radii imply that disorder can play a role in the stability and synthesizability of all-*d*-metal Heuslers; we save an accounting of such disorder effects for a future work.

Bain Paths and Magnetic Ground States. The magnetic ground state is a fundamental aspect for technological applications, for instance, the MCE in some Ni−Mn-X alloys involves AFM states, with strong dependence on the composition.[11] Meanwhile, different magnetic ground states can also lead to changes on the energy surface as a function of the c/a ratio, i.e., the Bain path. Correspondingly, we set out to not only verify the magnetic ground state for both the cubic and tetragonal phases but also check its changes with respect to the c/a ratio. Taking the 686 stable magnetic compounds, the Bain paths are calculated for both the inverse and regular Heusler structures in the FM state; concurrently, we evaluate the AFM Bain paths for compounds labeled as AFM based on HTP screening of possible prototypical AFM states (cf. Figure S.1), as detailed in the Methods section. The resulting magnetic ground states, symmetries, and lattice parameters for all the (meta-)stable compounds can be found in Table S.1. By comparing the AFM and FM Bain paths, we find 151 systems with an AFM ground state, 114 in the regular and 37 in the inverse Heusler settings. Of those confirmed to have an FM ground state, 354 (145) were regular (inverse) Heuslers. On the other hand, 468 out of 686 compounds are more stable with the tetragonal regular/inverse structure, which is in line with other studies that look at conventional Heusler alloys,[41] confirming that both the cubic and tetragonal structures should be considered in equal footing during HTP screening. Some compounds also prefer a ferrimagnetic arrangement, in particular inverse Heuslers tend to have a ferrimagnetic ordering when the A element is magnetic, due to its occupation of two distinct sublattices.[1]

Burch's Rule in All-*d*-Metal Heusler. A fundamental question is whether a Heusler compound stabilizes in regular or inverse structures and what is the underlying mechanism behind site-occupancy. In particular, for all-*d*-metal Heuslers several violations of Burch's occupancy rules have been noted, and a comprehensive understanding is warranted.[32,66] According to Burch's rule, the inverse Heusler structure is preferred if the A element is an earlier transition metal (TM) than the B element for A_2BC Heuslers.[8] The robustness of Burch's rule and DFT predictions was demonstrated by Kreiner et al., who compared both to available experimental data on 90 phases.[67] As such, our large HTP data set presents an ideal opportunity to study structure preference in the all-*d*-metal Heusler family. To this end, we plot in Figure 2a the histogram of our stable regular/inverse Heusler structures with respect to the difference between the periodic group numbers of the A and B elements. Likewise, Figure S.2a shows the distribution of the difference between the A and C element's group numbers; in the absence of main group elements, we label C as the element with the highest group number (excluding the well-defined A element). Clearly, there is a strong preference for the regular structure when the group number of the A element larger than that of other elements (large positive peak). However, the regular structure also dominates the extreme of the negative side (earlier period A element), with the inverse structure

https://doi.org/10.1021/acs.chemmater.4c00345
Chem. Mater. 2024, 36, 6765−6776

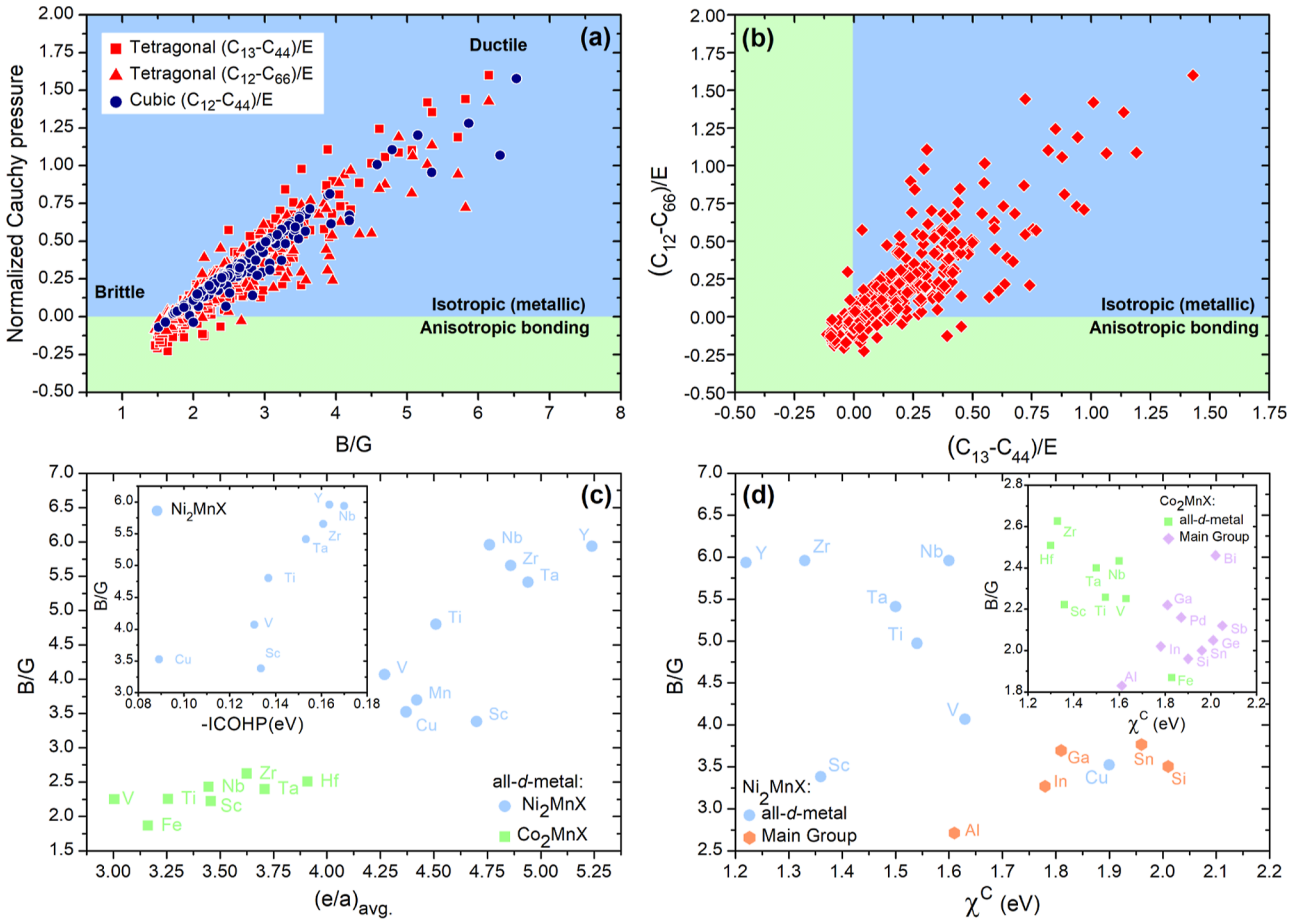

Figure 3. (a) Pugh ratio showing the brittle/ductile behavior versus the normalized Cauchy pressure which accounts for metallic or anisotropic nature. The cubic system is in blue circles and the two Cauchy pressures for the tetragonal systems are plotted separately as red triangles and squares. (b) The two Cauchy pressures for tetragonal systems plotted against each other, clarifying how many tetragonal systems are isotropic in each one. (c) Pugh ratio of hypothetical and stable all-*d*-metal Ni_2MnX and Co_2MnX cubic Heuslers versus the compositional average of e/a, the inset graph shows how the Pugh ratio scales with the bonding strength measured by the total -ICOHP averaged up to the third nearest-neighbors. (d) The Pugh ratios of the Ni_2MnX and Co_2MnX (in the inset) families compared to main group-based compounds as a function of the electronegativity of the X element. Data for Co_2MnX main group systems taken from Wu et al. Adapted with permission under a Creative Commons CC-BY 4.0 from 71. Copyright 2018 AIP Publishing.

being preferred around the middle. In short, the inverse structure seems to prefer small differences between the group numbers of A and B/C elements, and the Burch's rule does not fully apply.

To rationalize such results, we note that conventional Heusler compounds with a C main group element and Burch's rule imply that the regular structure is stabilized by the two rock-salt sublattices that coordinate the more electronegative/electropositive C/B elements with the A atom. In contrast, in the all-*d*-metal Heuslers, the regular structure is predominant when there is a small difference between the group numbers of A and B/C; hence, electronegativity difference tends to be smaller. As a way to describe the bonding in the inverse all-*d*-metal Heusler structures, we plot the electronegativity difference of A (χ^A) and of the average of B and C (χ^{BC}) in Figure 2b. We observe that in all-*d*-metal Heuslers the inverse setting tends to be preferred when $(\chi^A)-(\chi^{BC})$ is between roughly 0.1 and −0.2 eV, with the regular Heusler exhibiting two peaks (around −0.45 and 0.45 eV). This can be understood by recalling the Van Arkel-Ketelaar triangle, which indicates that in metallic and covalent bonding small differences in the electronegativity values are expected, as opposed to the large difference characteristic of ionic bonding.[68] Thus, in all-*d*-metal Heuslers, the inverse structure is preferred under small electronegativity difference, which favors the metallic bonding of the A-B and A′-C sublattices. To compare, we plot 108 experimentally reported main group based Heusler alloys in Figure 2c (listed in Table S.3), it is clear that Burch's rule is verified based on the negative inverse Heusler peak. Contrasting with the previous all-*d*-metal inverse Heuslers, those with main group elements in Figure 2b are predominant when $(\chi^A)-(\chi^{BC})$ is negative. Interestingly, there is a smaller peak in all-*d*-metal inverse Heuslers at −0.35 eV that matches the peak on the main group plot, hinting that there may be multiple overlapping bonding trends. We note that although we included tetragonal and cubic systems in the preceding analysis, the same trends are also verified in the subset of compounds that have a cubic ground state, as plotted in Figure S.2(b).

We further refine our explanation by noting that an inverse Heusler can be obtained by swapping the B element in the rock-salt with one of the simple-cubic A sites. In this substitutional picture the covalent radius mismatch of the solvent and solute elements should be considered as a key

https://doi.org/10.1021/acs.chemmater.4c00345
Chem. Mater. 2024, 36, 6765−6776

criterion, according to the Hume−Rothery rules.[69] As such, the difference between the covalent radius[70] of the A element (r^{A}_{cov}) and of the average radii of B and C (r^{BC}_{cov}) should not be too large. Putting the electronegativity and radius descriptors together, we map the structural preference between inverse and regular all-*d*-metal Heuslers in Figure 2e. It is clear that radius mismatch of the inverse structure is centered around 0.125, penalizing larger values. It is noted that outliers are expected, as we do not explicitly consider all bonds in the structures (such as AA' bonding), nor do we consider the valency of the elements. Nevertheless, we provided a simple picture as to the origin of inverse Heuslers in all-*d*-metal systems, while highlighting the metallic/covalent nature of the bonding in the all-*d*-metal Heusler family and explaining the violation of Burch's rules in all-*d*-metal Heusler alloys.

Mechanical Properties. To shed light on the mechanical stability and the unique mechanical properties of the all-*d*-metal Heusler alloys, we systematically evaluate their elastic constants (C_{ij}) and derive their moduli from the Voigt−Reuss−Hill method.[72] From the ab initio point of view, a key parameter is the Pugh ratio (B/G),[73] which describes the expected degree of brittleness/ductility of a compound, where B (G) is the bulk (shear) modulus. Typically, a reference value of 1.75 is taken as the start of ductile behavior;[74] however, Wu et al.[71] remarked that Co-based cubic Heuslers are above this value but are still brittle, as such we discuss the Pugh ratio in relative terms instead of a fixed threshold.

Another useful parameter, is Pettifor's Cauchy pressure, namely, $(C_{13}-C_{44})/E$ and $(C_{12}-C_{66})/E$ for tetragonal systems, and $C_{12}-C_{44})/E$ for cubic systems,[75,76] where E is the Young modulus. Here, positive values signal a metallic (isotropic) character, whereas a negative value implies more covalent/ionic (angular) bonding. Both Yan et al.[15] and Cong[16] et al. put forward that the higher Pugh ratio and larger positive Cauchy pressure of Ni−Mn−Ti in comparison to the conventional Ni−Mn-X Heusler alloys is a possible explanation for its better mechanical performance.

To highlight the broader behavior of the all-*d*-metal Heusler family, we plot both parameters in Figure 3a,b. It is immediately apparent that most compounds have large Pugh ratios, with a few being comparable with Ni_2MnTi (B/G = 4.97). While there are some (mostly tetragonal) that are brittle or with anisotropic bonding, most compounds are still labeled as metallic and ductile. These results suggest that the ductile/isotropic bonding behavior is a widespread feature of the all-*d*-metal Heusler family, likely owing to the composition including only TM elements.

Turning back to the mechanical behavior of Ni_2MnTi, it is worth noting that Ni_2MnX (X = Sn, Al, Ga, In, and Si) alloys with main group elements already have large Pugh ratios (between 2.71 and 3.77). This is higher than many of the compounds in our data set; thus, high Pugh ratios are hallmark of the Ni_2MnX system, which is then enhanced by specific TM elements, such as Ti. For comparison, Co_2MnX Heuslers with main group elements, which have been explored for spintronics applications, showcase Pugh ratios ranging from 1.96 to 2.46,[71] with their all-*d*-metal counterparts not showing enhanced ductile behavior, with ratios between 2.22 and 2.63. Huaxin et al.[28] remarked that partial replacement of Cu for Ti in Ni−Co−Mn−Ti results in a lower B/G ratio, in keeping with the lower value, we find for Ni_2MnCu of 3.5. Theoretical studies have sought to explain ductility in these compounds by assigning metallic character to the bonding based on Electron Localization Function.[15,34] However, this does not provide an explanation as to why the electronic character is more or less metallic among all-*d*-metal Heuslers, and as such, there is a need to understand how composition affects the mechanical behavior.

Heusler alloys are often discussed based on the number of valence electrons, for instance, the 24-electron-rule for semiconducting behavior[1] and e/a ratio when discussing structural transitions.[14] Given the metallic nature of all-*d* Heuslers, we discuss their ductility in terms of the elemental e/a ratios provided by Mizutani et al.,[77] which assigns a number to the electrons with an itinerant character from ab initio methods. Figure 3c plots the compositional average (labeled as $(e/a)_{avg}$) of Ni_2MnX and Co_2MnX cubic Heuslers against their Pugh ratios. It is observed that ductile behavior generally increases with the $(e/a)^{it.}_{avg}$ value, despite some deviation that is expected from the effect of local environment on the e/a. While conventional Ni_2MnX systems, seem insensitive to the e/a ratio (their e/a matches their valency), instead their ductility scales with increasing electronegativity as seen in Figure 3d. While conversely in the all-*d*-metal compounds, the ductility increases with smaller electronegativity, attesting to a difference in the underlying bonding behavior.

This behavior can be quantified using by integrating the Crystal Orbital Hamiltonian Populations (ICOHP),[50−52] which partitions the DFT band-structure into bonding (negative COHP) or antibonding (positive COHP) contributions, based on the Hamiltonian matrix element of a given pair of orbitals. Interestingly, in all-*d*-metal Ni_2MnX, the Pugh ratio increases with more negative ICOHP, indicating stronger bonding [inset of 3 (c)], with Ni-X and Mn-X contributions being the strongest contributions (not shown). Altogether, this indicates that the stronger *p*-*d* hybridization from a more electronegative main group element system results in stronger covalent bonding, leading to a more brittle behavior. Conversely, stronger *d*−*d* bonds in all-*d*-metal systems, due to the increasing number of itinerant electrons, result in a more ductile behavior.

Mechanical and Dynamical Stability. In addition to the thermodynamic stability criteria (E_f < 0, and ΔE_H < cutoff), both the dynamical (from phonon band structure) and mechanical (based on elastic constants[78]) stabilities should be evaluated, as described in the Methods section. Out of 686 compounds, most are stable in both criteria, with dynamical stability being the most stringent with 70 unstable compounds and 33 mechanically unstable (cf. Tables S.4, S.5).

Turning now to identifying Heusler compounds with the magneto-structural coupling needed for MCE and MSM, a typical double-well energy surface is expected along the Bain path, connecting a stable tetragonal and a (metastable) cubic structure.[10] Based on this criterion, we find 53 regular and 14 inverse Heusler compounds with a possible transition (aside from Ni_2MnTi). Among such 68 compounds, the most common case is FM states for both the martensite and austenite (cf., Table S.6). There are also 19 regular and 5 inverse systems exhibiting AFM ground state in either phase, with those compounds being mostly AFM in the martensite with a FM austenite, reflecting the previously observed trend. Regarding stability, the tetragonal martensite phase can be straightforwardly determined, i.e., dynamical and mechanical instabilities belie the existence of other more stable structures. In contrast, for the cubic austenite structures, imaginary phonon modes are known to occur in experimentally realized

https://doi.org/10.1021/acs.chemmater.4c00345
Chem. Mater. 2024, 36, 6765−6776

Table 1. Thermodynamic Stability of Compounds with Possible Transition with a Mechanically and Dynamically Stable Martensite, along with the Magnetic States and Moments (m) for Both Structures from Our Screening and the Energy Difference of the Austenite and Martensite

alloy	E_f [eV/atom]	ΔE_H [eV/atom]	$m^{Tetra.}$ [μB/atom]	c/a	state tetra	$m^{Cub.}$ [μB/atom]	state cub.	$E^{Cub.}-E^{Tetra.}$ [eV/atom]	type
Au_2MnCu	−0.059	0.029	1.03	1.22	FM	1.02	FM	0.001	reg.
Fe_2PtZn	−0.164	0.114	1.35	1.33	FM	1.34	FM	0.003	inv.
Zn_2CrRh	−0.117	0.131	0.92	1.37	FM	0.00	AFM	0.004	reg.
Co_2VMn	−0.099	0.067	0.23	1.42	FM	1.44	FM	0.004	reg.
Zn_2MnPd	−0.246	0.070	0.88	1.27	FM	0.89	FM	0.007	reg.
Ir_2MnZn	−0.195	0.000	0.00	1.28	AFM	0.78	FM	0.008	reg.
Mn_2NbIr	−0.170	0.100	0.00	1.45	AFM	1.18	FM	0.008	reg.
Fe_2MnPt	−0.078	0.092	0.00	1.37	AFM	2.25	FM	0.009	inv.
Pd_2MnAg	−0.146	0.034	1.11	1.26	FM	1.15	FM	0.010	reg.
Mn_2MoPt	−0.625	0.000	0.00	1.34	AFM	1.50	FM	0.011	reg.
Zn_2CrPt	−0.244	0.094	0.94	1.31	FM	0.83	FM	0.011	reg.
Fe_2IrCo	−0.019	0.039	0.00	1.35	AFM	2.15	FM	0.013	reg.
Zn_2HfMn	−0.082	0.121	0.36	1.45	FM	0.73	FM	0.014	reg.
Fe_2VRh	−0.128	0.094	0.95	1.44	FM	1.1	FM	0.016	inv.
Rh_2MnCu	−0.061	0.021	0.00	1.32	AFM	0.00	AFM	0.016	reg.
Fe_2TaIr	−0.239	0.099	1.01	1.46	FM	1.27	FM	0.017	inv.
Cu_2ZrMn	−0.014	0.147	0.53	1.49	FM	1.05	FM	0.019	reg.
Ni_2MnCu	−0.041	0.030	1.02	1.34	FM	1.06	FM	0.020	reg.
Zn_2MnRh	−0.249	0.000	1.02	1.38	FM	0.84	FM	0.021	reg.
Ti_2MnAu	−0.209	0.151	0.26	1.50	FM	0.45	FM	0.027	inv.
Pt_2MnCu	−0.309	0.000	1.01	1.31	FM	1.07	FM	0.037	reg.
Ir_2MnCu	−0.047	0.065	0.55	1.32	FM	0.57	FM	0.038	reg.
Fe_2TiPt	−0.399	0.065	1.04	1.47	FM	1.23	FM	0.046	inv.
Cu_2ScFe	−0.027	0.172	0.43	1.49	FM	0.57	FM	0.048	reg.
Zn_2TiMn	−0.131	0.071	0.26	1.52	FM	0.70	FM	0.048	reg.
Rh_2MnFe	−0.143	0.000	0.00	1.33	AFM	2.23	FM	0.052	reg.
Fe_2HfPt	−0.568	0.010	0.26	1.48	FM	1.26	FM	0.057	inv.
Co_2VFe	−0.109	0.054	0.78	1.39	FM	1.50	FM	0.061	reg.
Co_2NbFe	−0.054	0.086	0.79	1.37	FM	1.45	FM	0.062	reg.
Fe_2VIr	−0.209	0.058	0.00	1.40	AFM	1.01	FM	0.070	reg.
Co_2TaFe	−0.129	0.086	0.79	1.36	FM	1.40	FM	0.073	reg.
Mn_2TiPt	−0.387	0.074	0.15	1.46	AFM	0.42	AFM	0.077	inv.
Mn_2CoNi	−0.102	0.000	0.00	1.40	AFM	2.26	FM	0.084	reg.
Mn_2ReIr	−0.144	0.000	0.00	1.37	AFM	1.48	FM	0.086	reg.
Cu_2TiMn	−0.044	0.112	0.46	1.55	FM	0.98	FM	0.093	reg.
Mn_2CoPt	−0.256	0.000	0.00	1.38	AFM	2.26	FM	0.095	reg.
Mn_2TaPt	−0.279	0.099	0.00	1.51	AFM	1.23	FM	0.108	inv.
Mn_2RhCo	−0.158	0.000	0.00	1.39	AFM	2.03	FM	0.110	reg.
Mn_2RhPt	−0.383	0.000	0.00	1.33	AFM	2.26	FM	0.116	reg.
Ni_2NbMn	−0.158	0.076	0.58	1.47	FM	1.10	FM	0.116	reg.
Ni_2TaMn	−0.215	0.087	0.59	1.46	FM	1.06	FM	0.119	reg.
Mn_2RhNi	−0.217	0.000	0.00	1.39	AFM	2.24	FM	0.127	reg.
Fe_2MoIr	−0.058	0.104	0.88	1.44	FM	1.31	FM	0.128	inv.
Fe_2CrIr	−0.021	0.066	0.69	1.43	FM	1.65	FM	0.136	inv.
Mn_2IrCo	−0.206	0.000	0.00	1.33	AFM	2.00	FM	0.142	reg.
Ni_2VMn	−0.180	0.035	0.00	1.46	AFM	1.12	FM	0.169	reg.
Mn_2FeIr	−0.171	0.000	0.00	1.41	AFM	1.76	FM	0.170	reg.
Fe_2ReIr	−0.042	0.025	0.80	1.43	FM	1.44	FM	0.201	inv.
Mn_2WIr	−0.027	0.126	0.20	1.48	FM	1.20	FM	0.205	inv.

compounds, e.g., Ni_2MnGa, indicating that the martensite phase is more stable than the austenite phase.[10] Since the phonon spectra are obtained from T = 0 DFT calculations, thus we do not exclude the austenite phases with imaginary phonon modes, and discard only those compounds with unstable tetragonal structures. Based on these considerations, we find that 53 martensite structures are dynamically stable, while 62 are mechanically stable, resulting in 49 fully stable martensite structures shown in Table 1, and their Bain paths can be seen in Figures S.3 and S.4. Interestingly, several compounds are similar to systems with main group elements that have transitions, namely, the Ni_2MnX, Mn_2NiX, and Rh_2XY families.[79] The energy difference between the austenite and martensite ranges from a few meV, up to several hundred meV. Of note, Co_2VMn has been synthesized in the cubic phase,[23] despite the tetragonal state being 4 meV/atom lower

https://doi.org/10.1021/acs.chemmater.4c00345
Chem. Mater. 2024, 36, 6765−6776

than the cubic, indicating that small energy differences make determining a ground state difficult.

Structural Transitions. Magneto-structural coupling is a key factor for achieving a large magnetization change and thus enhancing MCE and MSM applications and enabling field control of the structural transition. The magneto-structural coupling can be quantified based on the concept of Curie temperature window (CTW), which has been previously applied to the experimental realization of a large MCE in the MM′X (M,M′ = metal, X = main group) family by disorder[80] and recently by us in the context of a computational workflow to search for novel MM′X.[44] In terms of CTW, the structural transitions should occur such that it involves two phases with different magnetizations, i.e., the structural phase transition temperature should lie in the temperature range spanned between the Curie temperatures of the martensite (T_C^{mart}) and austenite (T_C^{aust}) phases. Here, the CTW concept was extended in two ways. First, the austenite may be the high magnetization phase during the transition ($T_C^{aust} > T_C^{mart}$), leading to an inverse MCE. Second, a magneto-structural transition can also occur between AFM and FM states, in which case the upper limit of the window is the T_C of the FM phase.

To implement the CTW concept for screening magnetocaloric materials, it is essential to estimate the martensite transition temperature (T_M), the magnetic ground states of the martensite and austenite, and their respective magnetic ordering temperatures. The latter can be determined by using Monte Carlo simulations based on the exchange interactions calculated by DFT (more details in Methods). Meanwhile, the former requires an evaluation of the Gibbs free energy of the austenite and martensite phases and determining the temperature where the austenite becomes lower in free energy. To account for the Gibbs free energies, we include the vibrational (F^{vib}), electronic (F^{el}) using the quasi-harmonic approximation (volume dependent) and magnetic F(mag) contributions, which can be expressed as

$$F(T) = \min_V \{E_0(V) + F^{vib}(V, T) + F^{el}(V, T)\} + F^{mag}(T) \quad (1)$$

where E_0 are the T = 0 energies from DFT. Both $F^{vib}(V,T)$ and $F^{el}(V,T)$ contributions were calculated from DFT based on phonons and the electronic density of states, as detailed in Methods. As for $F^{(mag)}$, we applied the modified Inden−Hillert−Jarl (IHJ) model,[81] using the $T_{C/N}$ from our CTW calculation and the DFT moments, to keep calculations tractable we exclude the volume dependency. From the free energy, the T_M can be deduced by finding at what temperature austenite becomes the lowest energy structure.

Figure 4a plots the T_M (as red squares), where the compounds with 1400K denote that the martensite is always the lowest energy structure; hence, there is no predicted transition. The calculated CTW is also represented as an error bar in order to enable an easier comparison between values (cf., Table S.7). We note that this represents the case in absence of substitutional disorder, which commonly use to tune both the magnetic and structural transition temperatures. On the whole, we find 11 systems with a finite temperature structural transition, which we show in Table 2. Of all the free energy terms, the F^{vib} is the dominant term, with F^{mag} usually having a small effect of a few dozen Kelvin on the structural transition temperature. The exception is Pd_2MnAg, where the

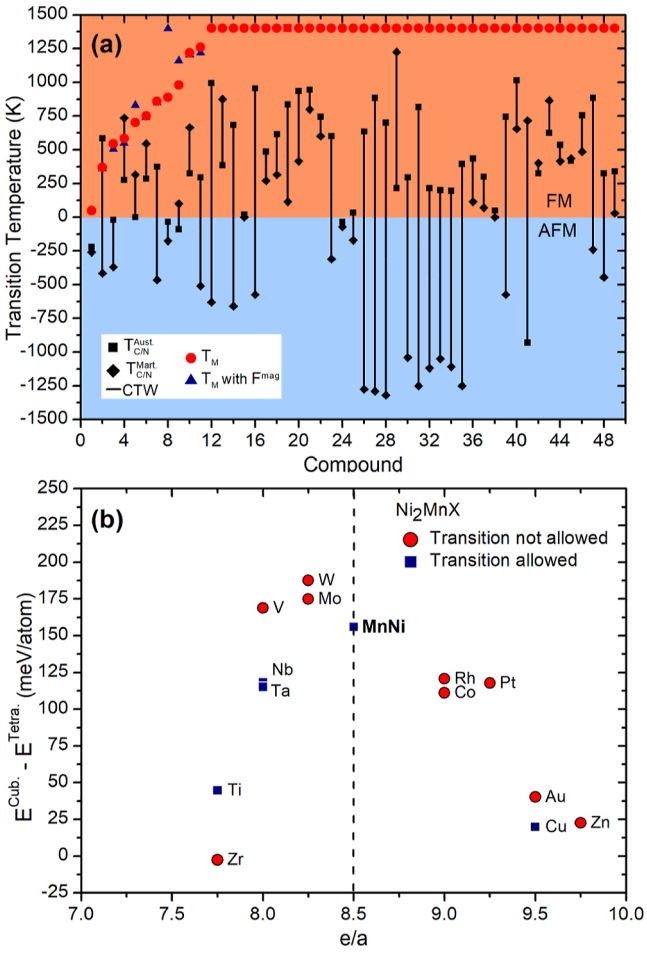

Figure 4. (a) Plot of the CTW represented as error bars, with the T_M calculated using all free energy terms as blue circles, with the red square marks being T_M without the magnetic contribution. (b) The e/a ratio of all-*D*-metal Ni_2MnX compounds vs the $E^{Cub}-E^{Tetra.}$ energy difference, including compounds that are only hypothetically stable in the regular and cubic structures. The blue squares are compounds with allowed transition from the Bain path, while the center line denotes the e/a value of MnNi.

martensite becomes more stable, and the transition is no longer observed. It is noteworthy that Ni_2NbMn, as a ligand, has a high Pugh ratio of 6.22. In this case, there is a wide CTW due to a high T_C martensite and a lower T_C austenite that is in line with a FM−PM transition; however, the high T_M precludes the possibility of magneto-structural transition without addition tuning, as we will discuss below. In the case of Zn_2MnPd, the transition lies squarely in the CTW, resulting in a predicted transition between an AFM martensite and FM austenite. Thus, the austenite is the high magnetization phase and the martensite is the low magnetization state, similar to Ni−Mn−In compounds that exhibit an inverse MCE.[12] In the case of Au_2MnCu, the T_M is too low and thermal arrest of the transition is expected.

Notably, we find that several compounds exhibit large volume differences between the cubic and tetragonal phases, which is a desirable feature for possible barocaloric applications. For instance, the all-*D*-metal Heusler alloy $Ni_{35.5}Co_{14.5}Mn_{35}Ti_{15}$ was found exhibit a strong barocaloric effect with high pressure sensitivity, owing to large volume change across the structural transition.[82] Based on DFT calculations, Guijiang Li and colleagues pointed out that

https://doi.org/10.1021/acs.chemmater.4c00345
Chem. Mater. 2024, 36, 6765−6776

Table 2. Systems with a Structural Transition at Finite Temperatures, with the Magnetic Néel/Curie Temperatures ($T_{C/N}$) along with the T_M with and without the F^{mag} Term and the Percentage of Volume Difference Between the Martensite and Austenite Phases. For Mechanically Stable Phases the Respective B/G Ratios Are Also Presented

alloy	ΔE_H [eV/atom]	$T^{Mart.}_{C/N}$ [K]	$T^{Aust.}_{C/N}$ [K]	T_M [K]	B/G aust	B/G mart	$\Delta v/v^{Aust.}$ (%)
Au_2MnCu	0.031	−260	−220	50/50	5.50	4.06	0.4
Zn_2MnPd	0.078	−415	585	360/370	3.67	2.50	0.8
Rh_2MnCu	0.021	−370	−20	505/545		2.27	−0.5
Cu_2ZrMn	0.147	735	275	550/585	3.48	3.52	−5.6
Zn_2HfMn	0.121	315	0	830/700	2.93	2.25	−2.2
Cu_2ScFe	0.172	545	285	740/750	8.13	3.29	−3.0
Mn_2TiPt	0.142	−465	375	850/860	3.96	2.17	−3.4
Pd_2MnAg	0.034	−175	−35	—/890	4.19	3.22	−0.6
Zn_2CrRh	0.131	100	−90	1160/980	2.50	2.44	−0.1
Ni_2NbMn	0.122	665	325	1205/1220	6.22	2.20	−4.7
Fe_2VIr	0.127	−510	295	1220/1260	3.82	1.70	−2.9

Ni2MnTi has large negative volume difference of −4%.[83] This is consistent with values for several of the compounds listed in Table 2. In particular, Ni2NbMn and Cu2ZrMn exhibit a volume difference of −4.7 and −5.6% respectively, comparing favorably to Ni2MnTi. In both cases, the magnetic moments of Mn in the austenite phase are significantly larger, for instance, 2.3 μ_B in the martensite of Ni2NbMn as opposed to 3.5 in the austenite phase. This hints at magneto-volume coupling as a factor behind the volume difference between phases.

Substitutional Tuning. Due to the stringent requirement of the T_M falling inside the CTW, a large MCE is typically accomplished by lowering the T_M or adjusting the CTW by substitutional disorder, as in the case of all-*d*-metal Ni−Co−Mn−Ti Heusler. Another strategy is isostructural substitution in the Mn(Ni,Co)(Ge,Si) MM'X alloy family, where one tunes toward a compound in the austenite phase (to control T_M) or toward a FM compound (to control the CTW).[80] As previously mentioned, in Heusler alloys, substitution is understood in terms of the number of valence electrons, where going way from the e/a of MnNi (8.5) lowers the transition temperature.[17] In the case of $Ni_2Mn_{1-x}Ti_x$, there is effectively an isostructural substitution of the NiMn alloy that has a high T_M of 973 K[84] toward an austenite ground state since the higher Ti content lowers T_M until the transition vanishes. At the same time, Co is added to manipulate the magnetic ground state and thus the CTW.[13,14]

This e/a ratio dependence can also be seen in Ni_2MnX all-*d*-metal compounds, as observed in Figure 4b that shows e/a versus the energy difference of the austenite and martensite under the assumption of a hypothetical regular Heusler structure. The compounds that are above or below the ratio of MnNi tend to have a lower energy difference between the phases, which in a first approximation would relate to the T_M.[85] However, the e/a ratio by itself does not account for the existence of a metastable austenite and stable martensite (compounds in blue squares).

As such, we propose to perform an isostructural substitution between a compound with an allowed transition and a compound stable in the austenite (martensite) to lower (increase) the $E^{Cub.}- E^{Tetra.}$, thus controlling the transition. This can be tested by calculating the Bain paths of compounds with substitutional disorder; to that end, we adopted the EMTO code using the CPA,[57−63] which we have previously applied to explain the experimental finding of long-range ordering in Ni−Co−Mn−Ti systems.[64] For instance, Ni_2VMn has a large energy difference between both states (0.169 eV/atom), while Co_2VMn is experimentally found in the austenite due to a small $E^{Cub.}- E^{Tetra.}$. Thus, the $Ni_{2-x}Co_xVMn$ isostructural substitution allows for the control of the Bain Path, as seen in Figure 5a. At around $Ni_{0.5}Co_{1.5}VMn$ (e/a = 6.125), the energy difference fully stabilizes the martensite, while the austenite is metastable, with a further increase of Nickel content increasing the energy difference, and by expectation T_M as desired. The same procedure can be used

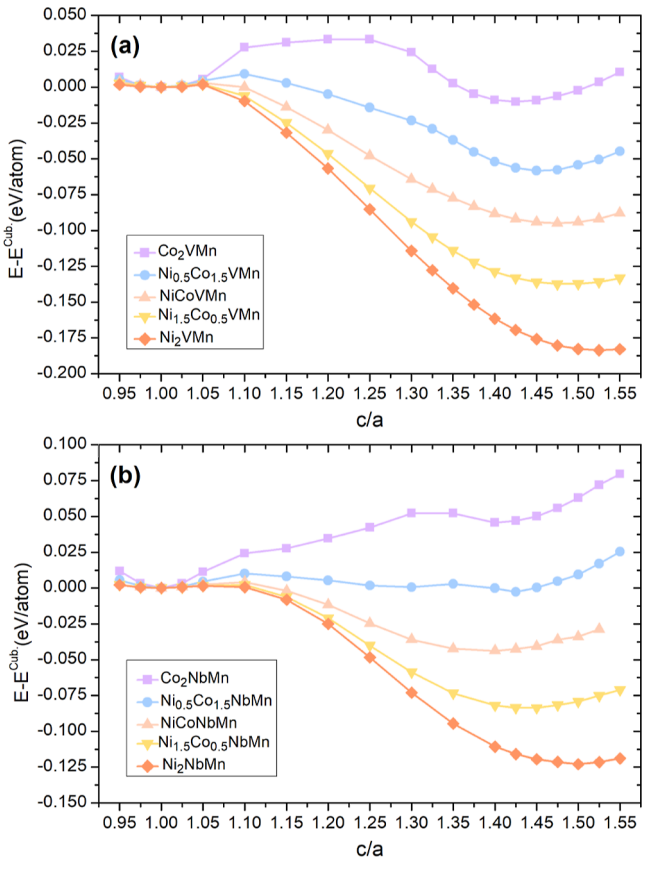

Figure 5. (a) Bain paths for $Ni_{2-x}Co_xVMn$ based on EMTO−CPA results. The values of energy are given in respect to the energy of the cubic austenite at each composition to allow a straightforward comparison of the energy difference with tetragonal martensite. (b) The Bain path for $Ni_{2-x}Co_xNbMn$.

https://doi.org/10.1021/acs.chemmater.4c00345
Chem. Mater. 2024, 36, 6765−6776

Ni_2NbMn by going toward the Co_2NbMn austenite phase, shown in Figure 5b. Once again, this allows control of the Bain path and thus the transition, demonstrating isostructural substitution as a method for tuning Heusler alloys and inducing magneto-structural coupling for MCE applications.

CONCLUSIONS

Based on HTP screening of all-*d*-metal Heusler alloys, we find 686 thermodynamically stable compounds, of which half is below 75 meV/atom above the convex Hull and the rest below 175 meV/atom. Based on our data set, we conclude that the inverse versus regular structural preference in all-*d*-metal Heusler alloys is driven by electronegativity difference between the A and B/C atoms, a low difference stabilizes the inverse structure, thus going against Burch's rule, which we honor with metallic bonding. Likewise based on Hume−Rothery rules, we show that a large mismatch of radius of B/C elements compared the A element favors the formation a regular structure, where the A element sits in its own sublattice. While Heusler alloys with main group elements prefer larger differences in electronegativity which favors an ionic bonding in the rock salt sublattice of the inverse Heusler. Following our HTP workflow for discovering materials with large MCE we establish possible structural transitions by calculating stable and metastable states in the form the FM and AFM Bain paths, we find 68 compounds with a double-well energy surface that allows or a structural transition, of these 49 are stable based on mechanical and dynamical stability criteria. Furthermore, by calculating finite-temperature magnetic behavior and free energies of both martensite and austenite phases we narrow down to 11 systems with a possible finite-temperature structural transition. Based on the concept of isostructural substitution, we provide a pathway to tune the transition in these novel Heusler systems.

ASSOCIATED CONTENT

Data Availability Statement

Further supporting data are available from the corresponding author, upon reasonable request.

Supporting Information

The Supporting Information is available free of charge at https://pubs.acs.org/doi/10.1021/acs.chemmater.4c00345.

Stability and lattice constants for all stable compounds, comparison between experimentally available phases and calculations, list of ground structure of main-group Heuslers, dynamically and mechanically unstable compounds, magnetic ground states of compounds with possible transitions and data of Figure 4a, magnetic ground states used for screening, structure preference of cubic compounds, and Bain paths of structures with allowed transitions (PDF)

AUTHOR INFORMATION

Corresponding Authors

Nuno M. Fortunato − *Institute of Materials Science, TU Darmstadt, 64287 Darmstadt, Germany; CICECO-Aveiro Institute of Materials, Department of Chemistry, University of Aveiro, 3810-193 Aveiro, Portugal;* orcid.org/0000-0002-9166-1626; Email: fortunato@tmm.tu-darmstadt.de

Hongbin Zhang − *Institute of Materials Science, TU Darmstadt, 64287 Darmstadt, Germany*; Email: hzhang@tmm.tu-darmstadt.de

Authors

Xiaoqing Li − *Department of Materials Science and Engineering, KTH - Royal Institute of Technology, SE-10044 Stockholm, Sweden*

Stephan Schönecker − *Department of Materials Science and Engineering, KTH - Royal Institute of Technology, SE-10044 Stockholm, Sweden*

Ruiwen Xie − *Institute of Materials Science, TU Darmstadt, 64287 Darmstadt, Germany*

Andreas Taubel − *Institute of Materials Science, TU Darmstadt, 64287 Darmstadt, Germany*

Franziska Scheibel − *Institute of Materials Science, TU Darmstadt, 64287 Darmstadt, Germany*

Ingo Opahle − *Institute of Materials Science, TU Darmstadt, 64287 Darmstadt, Germany*

Oliver Gutfleisch − *Institute of Materials Science, TU Darmstadt, 64287 Darmstadt, Germany*

Complete contact information is available at: https://pubs.acs.org/10.1021/acs.chemmater.4c00345

Author Contributions

H.Z. and O.G. conceived and led the research project, N.M.F performed the calculations with the assistance of X.L., S.S., and R.X. N.M.F and H.Z. wrote the draft. F.S., I.O., and A.T assisted in conceptualization. All coauthors contributed in the review and in providing feedback.

Notes

The authors declare no competing financial interest.

ACKNOWLEDGMENTS

We acknowledge the financial support from the European Research Council (ERC) under the European Union's Horizon 2020 research and innovation programme (grant no. 743116 - project" Cool Innov") and the Deutsche Forschungsgemeinschaft (DFG, German Research Foundation) - Project-ID 405553726 - TRR 270. Lichtenberg high performance computer of the TU Darmstadt where calculations were performed for this project is gratefully acknowledged for the computational resources.

REFERENCES

(1) Graf, T.; Felser, C.; Parkin, S. S. Simple rules for the understanding of Heusler compounds. *Prog. Solid State Chem.* **2011**, *39*, 1−50.

(2) Gutfleisch, O.; Willard, M. A.; Brück, E.; Chen, C. H.; Sankar, S. G.; Liu, J. P. Magnetic materials and devices for the 21st century: Stronger, lighter, and more energy efficient. *Adv. Mater.* **2011**, *23*, 821−842.

(3) Gutfleisch, O.; Gottschall, T.; Fries, M.; Benke, D.; Radulov, I.; Skokov, K. P.; Wende, H.; Gruner, M.; Acet, M.; Entel, P.; Farle, M. Mastering hysteresis in magnetocaloric materials. *Philos. Trans. R. Soc., A* **2016**, *374*, 20150308.

(4) Matsushita, Y. I.; Madjarova, G.; Dewhurst, J. K.; Shallcross, S.; Felser, C.; Sharma, S.; Gross, E. K. Large magnetocrystalline anisotropy in tetragonally distorted Heuslers: A systematic study. *J. Phys. D: Appl. Phys.* **2017**, *50*, 095002−095010.

(5) Planes, A.; Mañosa, L.; Acet, M. Magnetocaloric effect and its relation to shape-memory properties in ferromagnetic Heusler alloys. *J. Phys.: Condens. Matter* **2009**, *21*, 233201−233230.

(6) Palmstrøm, C. J. Heusler compounds and spintronics. *Prog. Cryst. Growth Charact. Mater.* **2016**, *62*, 371−397.

(7) Wollmann, L.; Nayak, A. K.; Parkin, S. S.; Felser, C. Heusler 4.0: Tunable Materials. *Annu. Rev. Mater. Res.* **2017**, *47*, 247−270.

(8) Burch, T. J.; Litrenta, T.; Budnick, J. I. Hyperfine Studies of Site Occupation in Ternary Systems. *Phys. Rev. Lett.* **1974**, *33*, 421−424.
(9) Bain, E. C. The Nature of Martensite. *Trans. Am. Inst. Min., Metall. Eng.* **1924**, *70*, 25−46.
(10) Entel, P.; Buchelnikov, V. D.; Khovailo, V. V.; Zayak, A. T.; Adeagbo, W. A.; Gruner, M. E.; Herper, H. C.; Wassermann, E. F. Modelling the phase diagram of magnetic shape memory Heusler alloys. *J. Phys. D: Appl. Phys.* **2006**, *39*, 865−889.
(11) Entel, P.; Gruner, M. E.; Fähler, S.; Acet, M.; Çahır, A.; Arróyave, R.; Sahoo, S.; Duong, T. C.; Talapatra, A.; Sandratskii, L.; et al. Probing Structural and Magnetic Instabilities and Hysteresis in Heuslers by Density Functional Theory Calculations. *Phys. Status Solidi B* **2018**, *255*, 1700296.
(12) Gottschall, T.; Skokov, K. P.; Benke, D.; Gruner, M. E.; Gutfleisch, O. Contradictory role of the magnetic contribution in inverse magnetocaloric Heusler materials. *Phys. Rev. B* **2016**, *93*, 184431−184437.
(13) Wei, Z. Y.; Liu, E. K.; Chen, J. H.; Li, Y.; Liu, G. D.; Luo, H. Z.; Xi, X. K.; Zhang, H. W.; Wang, W. H.; Wu, G. H. Realization of multifunctional shape-memory ferromagnets in all-d-metal Heusler phases. *Appl. Phys. Lett.* **2015**, *107*, 022406.
(14) Taubel, A.; Beckmann, B.; Pfeuffer, L.; Fortunato, N.; Scheibel, F.; Ener, S.; Gottschall, T.; Skokov, K. P.; Zhang, H.; Gutfleisch, O. Tailoring magnetocaloric effect in all-d-metal Ni-Co-Mn-Ti Heusler alloys: a combined experimental and theoretical study. *Acta Mater.* **2020**, *201*, 425−434.
(15) Yan, H. L.; Wang, L. D.; Liu, H. X.; Huang, X. M.; Jia, N.; Li, Z. B.; Yang, B.; Zhang, Y. D.; Esling, C.; Zhao, X.; Zuo, L. Giant elastocaloric effect and exceptional mechanical properties in an all-d-metal Ni−Mn−Ti alloy: Experimental and ab-initio studies. *Mater. Des.* **2019**, *184*, 108180.
(16) Cong, D.; Xiong, W.; Planes, A.; Ren, Y.; Mañosa, L.; Cao, P.; Nie, Z.; Sun, X.; Yang, Z.; Hong, X.; Wang, Y. Colossal Elastocaloric Effect in Ferroelastic Ni-Mn-Ti Alloys. *Phys. Rev. Lett.* **2019**, *122*, 255703.
(17) Wei, Z. Y.; Liu, E. K.; Li, Y.; Han, X. L.; Du, Z. W.; Luo, H. Z.; Liu, G. D.; Xi, X. K.; Zhang, H. W.; Wang, W. H.; Wu, G. H. Magnetostructural martensitic transformations with large volume changes and magneto-strains in all-d-metal Heusler alloys. *Appl. Phys. Lett.* **2016**, *109*, 071904.
(18) Neves Bez, H.; Pathak, A. K.; Biswas, A.; Zarkevich, N.; Balema, V.; Mudryk, Y.; Johnson, D. D.; Pecharsky, V. K. Giant enhancement of the magnetocaloric response in Ni−Co−Mn−Ti by rapid solidification. *Acta Mater.* **2019**, *173*, 225−230.
(19) Gottschall, T.; Gràcia-Condal, A.; Fries, M.; Taubel, A.; Pfeuffer, L.; Mañosa, L.; Planes, A.; Skokov, K. P.; Gutfleisch, O. A multicaloric cooling cycle that exploits thermal hysteresis. *Nat. Mater.* **2018**, *17*, 929−934.
(20) Liu, K.; Ma, S.; Ma, C.; Han, X.; Yu, K.; Yang, S.; Zhang, Z.; Song, Y.; Luo, X.; Chen, C.; Rehman, S. U.; Zhong, Z. Martensitic transformation and giant magneto-functional properties in all-d-metal Ni-Co-Mn-Ti alloy ribbons. *J. Alloys Compd.* **2019**, *790*, 78−92.
(21) Samanta, S.; Chatterjee, S.; Sinha, J.; Mandal, K. Giant reversibility of magnetoresponsive properties in all- d-metal Ni-Co-Mn(Cu)-Ti Heusler alloys: Role of phase-fraction-assisted magneto-structural transition. *Phys. Rev. Mater.* **2023**, *7*, 084406.
(22) Samanta, S.; Ghosh, S.; Mandal, K. Observation of giant exchange bias effect in Ni-Mn-Ti all-d-metal Heusler alloy. *J. Phys.: Condens. Matter* **2022**, *34*, 105801.
(23) Yu, M.; Li, G.; Fu, C.; Liu, E.; Manna, K.; Budiyanto, E.; Yang, Q.; Felser, C.; Tüysüz, H. Tunable eg Orbital Occupancy in Heusler Compounds for Oxygen Evolution Reaction. *Angew. Chem., Int. Ed.* **2021**, *60*, 5800−5805.
(24) de Paula, V. G.; Reis, M. S. All-d-Metal Full Heusler Alloys: A Novel Class of Functional Materials. *Chem. Mater.* **2021**, *33*, 5483−5495.
(25) Guan, Z.; Bai, J.; Gu, J.; Liang, X.; Liu, D.; Jiang, X.; Huang, R.; Zhang, Y.; Esling, C.; Zhao, X.; Zuo, L. First-principles investigation of B2 partial disordered structure, martensitic transformation, elastic and magnetic properties of all-d-metal Ni-Mn-Ti Heusler alloys. *J. Mater. Sci. Technol.* **2021**, *68*, 103−111.
(26) Ni, Z.; Guo, X.; Liu, X.; Jiao, Y.; Meng, F.; Luo, H. Understanding the magnetic structural transition in all-d-metal Heusler alloy Mn2Ni1.25Co0.25Ti0.5. *J. Alloys Compd.* **2019**, *775*, 427−434.
(27) Zeng, Q.; Shen, J.; Zhang, H.; Chen, J.; Ding, B.; Xi, X.; Liu, E.; Wang, W.; Wu, G. Electronic behaviors during martensitic transformations in all-d-metal Heusler alloys. *J. Phys.: Condens. Matter* **2019**, *31*, 425401.
(28) Qi, H.; Bai, J.; Jin, M.; Xu, J.; Liu, X.; Guan, Z.; Gu, J.; Cong, D.; Zhao, X.; Zuo, L. First-principles calculations of Ni-(Co)-Mn-Cu-Ti all-d-metal Heusler alloy on martensitic transformation, mechanical and magnetic properties. *Int. J. Miner., Metall. Mater.* **2023**, *30*, 930−938.
(29) Xiong, C.; Bai, J.; Li, Y.; Gu, J.; Liang, X.; Guan, Z.; Zhang, Y.; Esling, C.; Zhao, X.; Zuo, L. First-Principles Investigation on Phase Stability, Elastic and Magnetic Properties of Boron Doping in Ni-Mn-Ti Alloy. *Acta Metall. Sin. (Engl. Lett.)* **2022**, *35*, 1175−1183.
(30) Zhang, F.; Batashev, I.; van Dijk, N.; Brück, E. Reduced Hysteresis and Enhanced Giant Magnetocaloric Effect in B-Doped all-d-Metal Ni-Co-Mn-Ti-Based Heusler Materials. *Phys. Rev. Appl.* **2022**, *17*, 054032.
(31) Wu, M.; Zhou, F.; Khenata, R.; Kuang, M.; Wang, X. Phase Transition and Electronic Structures of All-d-Metal Heusler-Type X2MnTi Compounds (X = Pd, Pt, Ag, Au, Cu, and Ni). *Front. Chem.* **2020**, *8*, 546947.
(32) Han, Y.; Wu, M.; Feng, Y.; Cheng, Z.; Lin, T.; Yang, T.; Khenata, R.; Wang, X. Competition between cubic and tetragonal phases in all-*d*-metal Heusler alloys, $X_{2-x}Mn_{1+x}V$ (X = Pd, Ni, Pt, Ag, Au, Ir, Co; x = 1, 0): a new potential direction of the Heusler family. *IUCrJ.* **2019**, *6*, 465−472.
(33) Han, Y.; Bouhemadou, A.; Khenata, R.; Cheng, Z.; Yang, T.; Wang, X. Prediction of possible martensitic transformations in all-d-metal Zinc-based Heusler alloys from first-principles. *J. Magn. Magn. Mater.* **2019**, *471*, 49−55.
(34) Li, G.; Liu, E.; Wang, W.; Wu, G. Theoretical investigations on elastic properties, phase stability, and magnetism in Ni2Mn-based all-d-metal Heusler compounds. *Phys. Rev. B* **2023**, *107*, 134440.
(35) Jiang, S.; Yang, K. Review of high-throughput computational design of Heusler alloys. *J. Alloys Compd.* **2021**, *867*, 158854.
(36) Zhang, H. High-throughput Design of Magnetic Materials. *Electron. Struct.* **2021**, *3*, 033001.
(37) Sanvito, S.; Oses, C.; Xue, J.; Tiwari, A.; Zic, M.; Archer, T.; Tozman, P.; Venkatesan, M.; Coey, M.; Curtarolo, S. Accelerated discovery of new magnets in the Heusler alloy family. *Sci. Adv.* **2017**, *3*, No. e1602241.
(38) Balluff, J.; Diekmann, K.; Reiss, G.; Meinert, M. High-throughput screening for antiferromagnetic Heusler compounds using density functional theory. *Phys. Rev. Mater.* **2017**, *1*, 034404.
(39) Kirklin, S.; Saal, J. E.; Hegde, V. I.; Wolverton, C. High-throughput computational search for strengthening precipitates in alloys. *Acta Mater.* **2016**, *102*, 125−135.
(40) He, J.; Amsler, M.; Xia, Y.; Naghavi, S. S.; Hegde, V. I.; Hao, S.; Goedecker, S.; Ozoliņš, V.; Wolverton, C. Ultralow Thermal Conductivity in Full Heusler Semiconductors. *Phys. Rev. Lett.* **2016**, *117*, 046602.
(41) Faleev, S. V.; Ferrante, Y.; Jeong, J.; Samant, M. G.; Jones, B.; Parkin, S. S. Origin of the Tetragonal Ground State of Heusler Compounds. *Phys. Rev. Appl.* **2017**, *7*, 034022.
(42) Oliynyk, A. O.; Antono, E.; Sparks, T. D.; Ghadbeigi, L.; Gaultois, M. W.; Meredig, B.; Mar, A. High-Throughput Machine-Learning-Driven Synthesis of Full-Heusler Compounds. *Chem. Mater.* **2016**, *28*, 7324−7331.
(43) Tanzim, M. F.; Fortunato, N.; Samathrakis, I.; Xie, R.; Opahle, I.; Gutfleisch, O.; Zhang, H. Giant anomalous Hall and Nernst conductivities in magnetic all-*d* metal Heusler alloys. *Adv. Funct. Mater.* **2023**, *33*, 2214967.

https://doi.org/10.1021/acs.chemmater.4c00345
Chem. Mater. 2024, 36, 6765−6776

(44) Fortunato, N. M.; Taubel, A.; Marmodoro, A.; Pfeuffer, L.; Ophale, I.; Ebert, H.; Gutfleisch, O.; Zhang, H. High-Throughput Design of Magnetocaloric Materials for Energy Applications: MMX alloys. *Adv. Sci.* **2023**, *10*, 2206772.
(45) Kresse, G.; Furthmüller, J. Efficient iterative schemes for ab initio total-energy calculations using a plane-wave basis set. *J. Phys. Chem. A* **1996**, *54*, 11169−11186.
(46) Kresse, G.; Furthmüller, J. Efficiency of ab-initio total energy calculations for metals and semiconductors using a plane-wave basis set. *Comput. Mater. Sci.* **1996**, *6*, 15−50.
(47) Singh, H. K.; Zhang, Z.; Opahle, I.; Ohmer, D.; Yao, Y.; Zhang, H. High-Throughput Screening of Magnetic Antiperovskites. *Chem. Mater.* **2018**, *30*, 6983−6991.
(48) Perdew, J. P.; Burke, K.; Ernzerhof, M. Generalized gradient approximation made simple. *Phys. Rev. Lett.* **1996**, *77*, 3865−3868.
(49) Togo, A.; Tanaka, I. First principles phonon calculations in materials science. *Scr. Mater.* **2015**, *108*, 1−5.
(50) Dronskowski, R.; Bloechl, P. E. Crystal orbital hamilton populations (COHP). Energy-resolved visualization of chemical bonding in solids based on density-functional calculations. *J. Phys. Chem.* **1993**, *97*, 8617−8624.
(51) Maintz, S.; Deringer, V. L.; Tchougréeff, A. L.; Dronskowski, R. LOBSTER: A tool to extract chemical bonding from plane-wave based DFT. *J. Comput. Chem.* **2016**, *37*, 1030−1035.
(52) Maintz, S.; Deringer, V. L.; Tchougréeff, A. L.; Dronskowski, R. Analytic projection from plane-wave and PAW wavefunctions and application to chemical-bonding analysis in solids. *J. Comput. Chem.* **2013**, *34*, 2557−2567.
(53) Liechtenstein, A.; Katsnelson, M.; Antropov, V.; Gubanov, V. Local Spin Density Functional Approach to the Theory of Exchange Interactions in Ferromagnetic Metals and Alloys. *J. Magn. Magn. Mater.* **1987**, *67*, 65−74.
(54) Ebert, H.; Ködderitzsch, D.; Minár, J. Calculating condensed matter properties using the KKR-Green's function method - Recent developments and applications. *Rep. Prog. Phys.* **2011**, *74*, 096501.
(55) Ebert, H. The munich spr-kkr package, version 7.7. https://www.ebert.cup.uni-muenchen.de/index.php/de/software/13-sprkkwebr, 2022 (accessed Mar 15, 2022).
(56) Developers, T. J. K. The Julich KKR Codes. https://jukkr.fz-juelich.deweb/, 2021 (accessed July 22, 2021).
(57) Andersen, O.; Jepsen, O.; Krier, G.. In *Lectures on Methods of Electronic Structure Calculations* Kumar, V., Andersen, O. K., Mookerjee, A., Eds.; World Scientific Publishing Co., 1994; pp 63−124.
(58) Kollar, J.; Vitos, L.; Skriver, H. L.. In *Lecture Notes in Physics: Electronic Structure and Physical Properties of Solids* Dreysse, H., Ed.; Springer-Verlag, 2000; .
(59) Vitos, L. *Computational Quantum Mechanics for Materials Engineers: The EMTO Method and Applications*; Springer-Verlag, 2007; .
(60) Vitos, L.; Skriver, H. L.; Johansson, B.; Kollár, J. Application of the exact muffin-tin orbitals theory: the spherical cell approximation. *Comput. Mater. Sci.* **2000**, *18*, 24−38.
(61) Vitos, L. Total-energy method based on the exact muffin-tin orbitals theory. *Phys. Rev. B: Condens. Matter Mater. Phys.* **2001**, *64*, 014107.
(62) Vitos, L.; Kollár, J.; Skriver, H. L. Full charge-density scheme with a kinetic-energy correction: Application to ground-state properties of the 4d metals. *Phys. Rev. B* **1997**, *55*, 13521−13527.
(63) Vitos, L.; Abrikosov, I. A.; Johansson, B. Anisotropic lattice distortions in random alloys from first-principles theory. *Phys. Rev. Lett.* **2001**, *87*, 156401.
(64) Koch, D.; Beckmann, B.; Fortunato, N. M.; Miroshkina, O. N.; Gruner, M. E.; Zhang, H.; Gutfleisch, O.; Donner, W. Chemical long range ordering in all-d-metal Heusler alloys. *J. Appl. Phys.* **2022**, *131*, 073903.
(65) Graf, T.; Casper, F.; Winterlik, J.; Balke, B.; Fecher, G. H.; Felser, C. Crystal structure of new heusler compounds. *Z. fur Anorg. Allg. Chem.* **2009**, *635*, 976−981.
(66) Bachagha, T.; Suñol, J. J. All-d-Metal Heusler Alloys: A Review. *Metals* **2023**, *13*, 111.
(67) Kreiner, G.; Kalache, A.; Hausdorf, S.; Alijani, V.; Qian, J. F.; Shan, G.; Burkhardt, U.; Ouardi, S.; Felser, C. New Mn2-based Heusler compounds. *Z. fur Anorg. Allg. Chem.* **2014**, *640*, 738−752.
(68) Norman, N. C. *Periodicity and the s- and p-Block Elements; Oxford Chemistry Primers*; Oxford University Press, 1997.
(69) Mizutani, U. *Hume-Rothery Rules for Structurally Complex Alloy Phases*, 1st ed.; CRC Press, 2010.
(70) Haynes, W. M. *CRC Handbook of Chemistry and Physics*, 97th ed.; CRC Press, 2016.
(71) Wu, S. C.; Fecher, G. H.; Shahab Naghavi, S.; Felser, C. Elastic properties and stability of Heusler compounds: Cubic Co 2 YZ compounds with L 2 1 structure. *J. Appl. Phys.* **2019**, *125*, 082523.
(72) Hill, R. The Elastic Behaviour of a Crystalline Aggregate. *Proc. Phys. Soc., Sect. A* **1952**, *65*, 349−354.
(73) Pugh, S. XCII. Relations between the elastic moduli and the plastic properties of polycrystalline pure metals. *London, Edinburgh Dublin Philos. Mag. J. Sci.* **1954**, *45*, 823−843.
(74) Niu, H.; Chen, X. Q.; Liu, P.; Xing, W.; Cheng, X.; Li, D.; Li, Y. Extra-electron induced covalent strengthening and generalization of intrinsic ductile-to-brittle criterion. *Sci. Rep.* **2012**, *2*, 718.
(75) Born, M.; Huang, K. *Dynamical Theory of Crystal Lattices; the International Series of Monographs on Physics*, 1998; .
(76) Pettifor, D. G. Theoretical predictions of structure and related properties of intermetallics. *Mater. Sci. Technol.* **1992**, *8*, 345−349.
(77) Mizutani, U.; Sato, H. The physics of the Hume-Rothery electron concentration rule. *Crystals* **2017**, *7*, 9.
(78) Mouhat, F.; Coudert, F. X. Necessary and sufficient elastic stability conditions in various crystal systems. *Phys. Rev. B* **2014**, *90*, 224104.
(79) Wu, Q. S.; Zhang, S. N.; Song, H. F.; Troyer, M.; Soluyanov, A. A. WannierTools: An open-source software package for novel topological materials. *Comput. Phys. Commun.* **2018**, *224*, 405−416.
(80) Wei, Z. Y.; Liu, E. K.; Li, Y.; Xu, G. Z.; Zhang, X. M.; Liu, G. D.; Xi, X. K.; Zhang, H. W.; Wang, W. H.; Wu, G. H.; Zhang, X. X. Unprecedentedly Wide Curie-Temperature Windows as Phase-Transition Design Platform for Tunable Magneto-Multifunctional Materials. *Adv. Electron. Mater.* **2015**, *1*, 1500076.
(81) Xiong, W.; Chen, Q.; Korzhavyi, P. A.; Selleby, M. An improved magnetic model for thermodynamic modeling. *CALPHAD: Comput. Coupling Phase Diagrams Thermochem.* **2012**, *39*, 11−20.
(82) Wei, Z.; Shen, Y.; Zhang, Z.; Guo, J.; Li, B.; Liu, E.; Zhang, Z.; Liu, J. Low-pressure-induced giant barocaloric effect in an all-d-metal Heusler Ni35.5Co14.5Mn35Ti15magnetic shape memory alloy. *APL Mater.* **2020**, *8*, 051101.
(83) Li, G.; Liu, E.; Wu, G. d-d hybridization controlled large-volume-change martensitic phase transition in Ni-Mn-Ti-based all-d-metal Heusler compounds. *J. Alloys Compd.* **2022**, *923*, 166369.
(84) Potapov, P. L.; Polyakova, N. A.; Udovenko, V. A.; Svistunova, E. L. The Martensitic Structure and Shape Memory Effect in NiMn Alloyed by Ti and Al. *Int. J. Mater. Res.* **1996**, *87*, 33−39.
(85) Barman, S. R.; Chakrabarti, A.; Singh, S.; Banik, S.; Bhardwaj, S.; Paulose, P. L.; Chalke, B. A.; Panda, A. K.; Mitra, A.; Awasthi, A. M. Theoretical prediction and experimental study of a ferromagnetic shape memory alloy: Ga2MnNi. *Phys. Rev. B* **2008**, *78*, 134406.

https://doi.org/10.1021/acs.chemmater.4c00345
Chem. Mater. 2024, 36, 6765−6776